Electrical and Optical Characterization of Atmospheric-Pressure Helium Plasma Jets Generated With a Pin Electrode: Effects of the Electrode Material, Ground Ring Electrode, and Nozzle Shape

Hea Min Joh, Hae Ra Kang, Tae Hun Chung, and Sun Ja Kim

***Abstract*— This paper tests various design and operation parameters in atmospheric-pressure helium plasma jets generated with a pin electrode to provide a plasma environment well suited for material processing or biomedical applications. The effects of the pin electrode materials (Cu, W, and Al), the position, and the width of a ground ring electrode on the characteristics of the jets are studied. The inner quartz tube encompassing the pin electrode and two types of the outer quartz tubes (straight or tapered cylinder shape) are employed, and their effects are investigated. The electrical characteristics of the plasma jets are measured by current–voltage measurements and analyzed by the equivalent circuit model. The optical characteristics of the discharges are obtained by optical emission spectroscopy to identify various excited plasma species produced in the plasma jets. Optical emission spectra are also obtained at different positions along the coaxial direction. A variety of choices in design parameters and operation parameters are undertaken to determine optimal conditions and elucidate the properties of the plasma jets.**

***Index Terms*— Atmospheric-pressure plasma (APP) jet, equivalent circuit model of plasma jets, pin electrode, plasma plume.**

I. Introduction

NONEQUILIBRIUM atmospheric-pressure plasmas (APPs) have drawn intense interest in current low-temperature plasma research because of their immense potential for material processing and biomedical applications [1]. The advantage of APPs is that, while providing a significant number of active species, such as radicals, electrons, and ions, the gas can be maintained at room temperature. A low gas temperature is an essential feature in the application of plasmas in the fields of biology and medicine and in treating thermally sensitive materials because it ensures less damage to samples. In particular, APP jet sources can produce local nonthermal plasma, characterized by flexibility, compactness, and efficiency. Since APP jets generate plasma plumes in open space surrounding air rather than in confined discharge gaps, they can be used for direct treatment and there are no limitations on the sizes of the objects to be treated.

The plasma generation in APP jets relies on various mechanisms: corona discharge, streamer discharge, and dielectric barrier discharge (DBD) [2]–[6]. Corona discharges appear as a luminous glow localized in space around a point tip (or wire) in a highly nonuniform electric field. DBDs operating at atmospheric pressure are driven by a pulsed or sinusoidal voltage at frequencies from 50 Hz up to several tens of kilohertz (even up to RF), and at least one of the electrodes has an insulating layer. Physically, the breakdown mechanism of APP jets strongly depends on electron multiplication, which controls the transition from Townsend breakdown to streamer breakdown [7]–[12]. When operating at lower frequencies, the plasma jet was found to be constituted of discrete plasma bullets moving at a velocity much higher than the gas velocity [9]–[13]. The propagation is sustained by photoionization [7], [10]–[12]. First, the electrons are accelerated toward the positive ions, and then the photons are emitted. These photons produce new photoelectrons and positive ions at a suitable distance; therefore, the plasma bullet's ionization front starts propagating with the successful completion of these events. The high electric field between the photoelectron and positive streamer tip results in a rapid acceleration of the electron, thus producing an avalanche [7], [13].

As the plasma bullet travels to further distances, it leaves behind a channel consisting of short- and long-lived species. A secondary discharge is ignited at the end of the applied voltage pulse (or a falling phase of sinusoidal voltage) due to the charge accumulation on the dielectric electrode surface. This newly formed discharge interrupts the plasma bullet propagation. This opposing jet current (negative current) occurring at the end of the applied voltage pulse (or a falling phase of sinusoidal voltage) is due to the acceleration of electrons that arose from the secondary discharge toward the plasma

Manuscript received February 24, 2014; revised May 15, 2014; accepted June 18, 2014. Date of publication July 8, 2014; date of current version December 9, 2014. This work was supported by the National Research Foundation of Korea under Contract 2012R1A1A2002591.

The authors are with the Department of Physics, Dong-A University, Busan 604-714, Korea (e-mail: dkwk1920@naver.com; haera_@hanmail.net; thchung@dau.ac.kr; sjkim@dau.ac.kr).

Color versions of one or more of the figures in this paper are available online at http://ieeexplore.ieee.org.

Digital Object Identifier 10.1109/TPS.2014.2332171

0093-3813 © 2014 IEEE. Personal use is permitted, but republication/redistribution requires IEEE permission.
See http://www.ieee.org/publications_standards/publications/rights/index.html for more information.

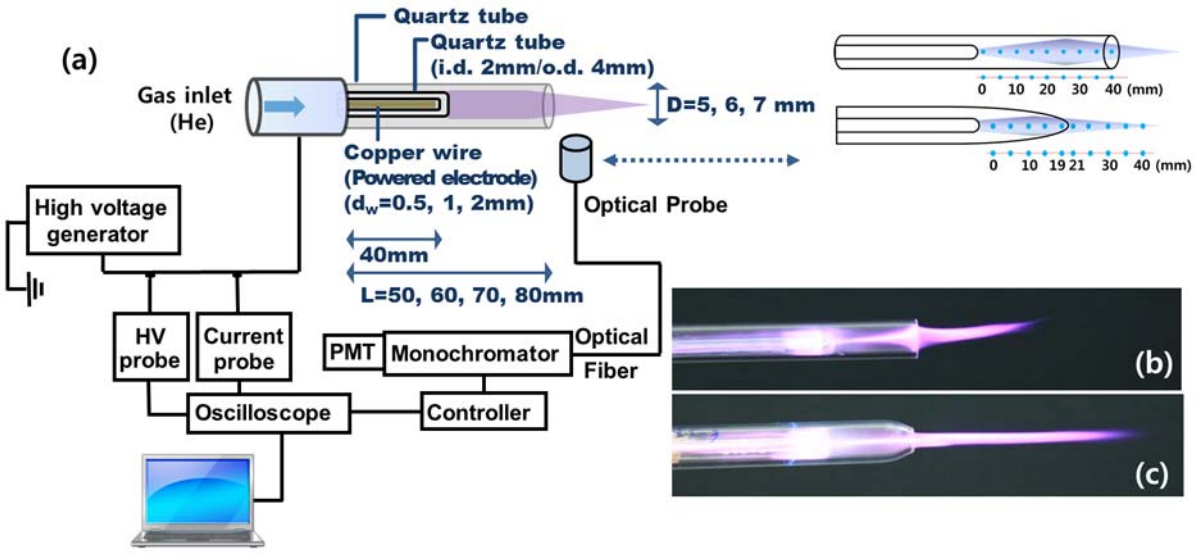

Fig. 1. (a) Schematics of the experimental setup. Photographs of the plumes from (b) straight cylinder type and (c) tapered type jets.

bullet as a result of the electric field established by the charges accumulated on the dielectric surface. This opposing motion of electrons cancels out the positive charges of the plasma bullet. Therefore, the electric field between photoelectrons and the head of the plasma bullet becomes very small, and no further avalanche occurs. Hence, the plasma bullet stops propagating [10].

The devices developed in this paper also utilize the combined working principles of corona discharge, streamer discharge, and DBD. Atmospheric-pressure cold plasma jets represent a rapidly developing technology of great application promise. Obviously, the employment of pin electrodes is favorable to produce a stronger electric field at moderate applied voltages. With a large local curvature of the pin point and a short distance between the electrode pair, the generated electric field is sufficiently high to induce the breakdown and sustain the resulting plasma at relatively moderate applied voltage.

For biomedical applications, APP sources should meet two common criteria: 1) generation and transport of abundant reactive species near room temperature and 2) remote treatment to minimize electric shock, current-induced heating, and arcing. In this paper, plasma jets with a pin electrode are fabricated under various design configurations and characterized to provide a plasma environment well suited for the treatment of thermally sensitive materials and biomedical materials. The effects of the various design configurations and operation parameters on the discharge properties of plasma are investigated. The effects of the pin electrode materials (Cu, W, and Al), the position, and the width of a ground ring electrode on the characteristics of the jets are studied. The effects of an inner quartz tube encompassing the pin electrode and two types of the outer quartz tubes (straight or tapered cylinder shape) are investigated. The physical properties of the generated plume include the current–voltage (I–V) characteristics, plume temperatures, plume length, and species compositions deduced from optical emission spectroscopy. Particular attention is paid to the electrical characterization based on the equivalent circuit model.

II. Experiment

The plasma jet device in this paper consisted of a quartz confinement tube [outer quartz tube of straight or tapered (funnel-shaped) cylinder] and a pin electrode (Cu unless otherwise stated) surrounded by an inner quartz tube with right end closed. This device was designed with some modifications to the plasma jet introduced in [14]. A schematic diagram is shown in Fig. 1(a). A quartz confinement tube (inner diameter D = 5, 6, and 7 mm; length L = 5–80 mm) served as the dielectric barrier layer. Without the ring electrode, the dielectric tube only plays the role of guiding the gas flow. The jet had a central powered electrode (copper pin wire of diameters d_w = 0.5, 1.0, and 2.0 mm) The pin electrode can either be bare or be inserted in an inner quartz tube. High-purity helium (99.997%) was used as the discharge gas. The photographs of the plumes from a straight cylinder type jet and a tapered type jet are shown in Fig. 1(b) and (c), respectively.

A small diameter of the pin electrode with a sharp edge allowed for a local enhancement of the electric field and, thus, a considerable reduction of the breakdown voltage requirement. The plasma was generated by a pulsed bipolar source with a repetition frequency of several tens of kilohertz (EESYS APPS020). A typical operation condition of the plasma jet had an applied voltage of 1.9 kV_{rms} (root-mean-square value), a repetition frequency of 50 kHz, and a pulsewidth of 5.5 μs. The waveforms of the voltage and the current were measured using a real-time digital oscilloscope (LeCroy WS44XS-A) via high-voltage probe (Tektronix P5100) and current probe (Pearson 3972). To identify reactive species generated in the discharge and subsequently expelled with the gas flow, optical spectra were recorded for emission in the range of 200–900 nm. The emission was collected perpendicular to the plume's propagating direction at several measurement points (z) along the axis of the jets (straight or tapered

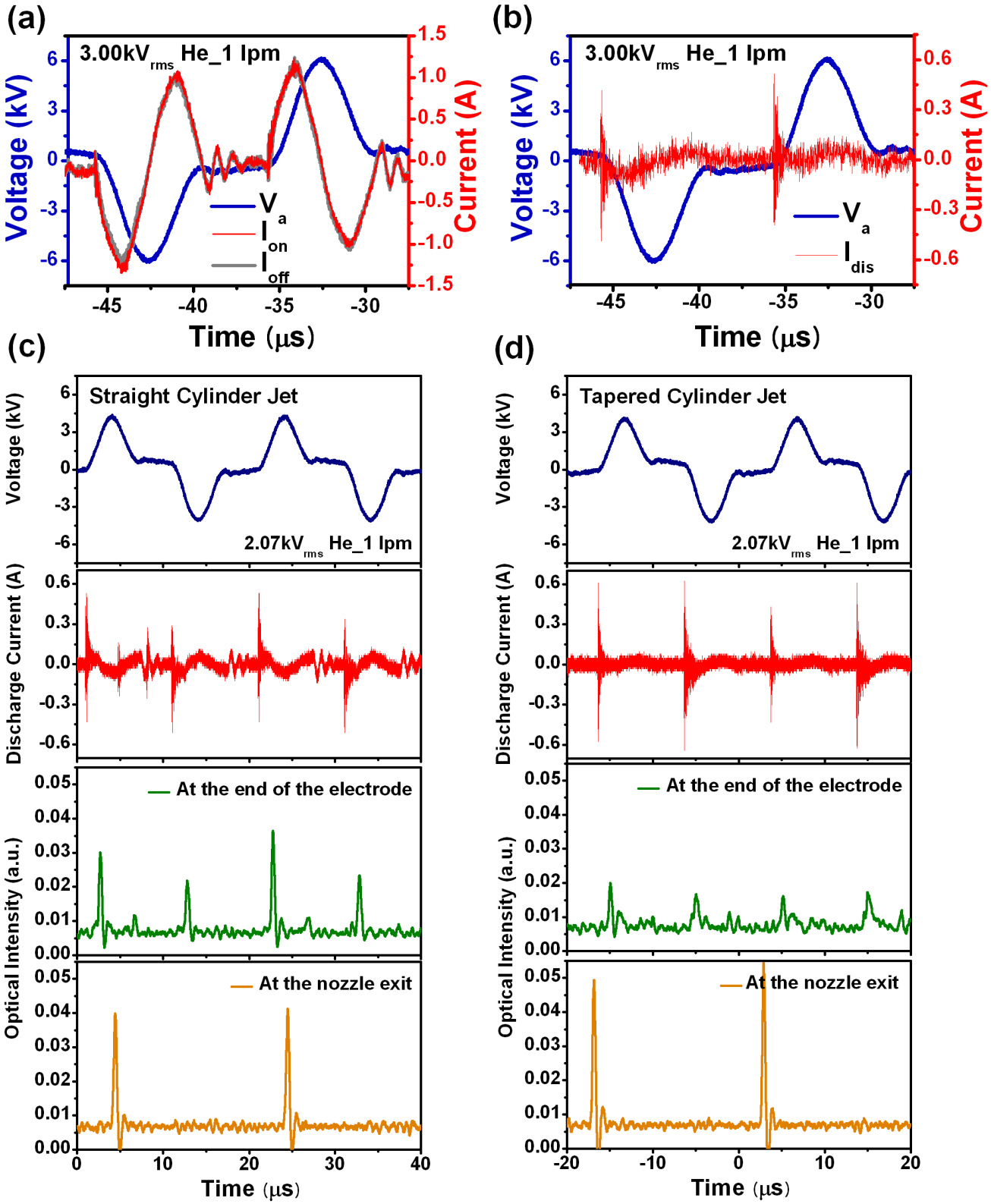

Fig. 2. Waveforms of the applied voltages. (a) Total current and (b) discharge current for the jets driven by a pulsed bipolar source at 50 kHz. Temporal evolutions of the wavelength-integrated optical emission intensity for two types of outer tubes (c) straight cylinder jet and (d) tapered jet.

cylinder), as shown in Fig. 1. The light emitted by the plasma was focused by means of optical fiber into the entrance slit of a 0.75-m monochromator (SPEX 1702), equipped with a grating of 1200 grooves/mm and a slit width of 100 μm. To verify the general optical properties of the plasma jets, the optical emissions were measured as a function of time. A photosensor amplifier (Hamamatsu C6386-01) was used to observe the wavelength-integrated plasma emission.

III. Results and Discussion

A. Electrical Characteristics and Plume Generation

Fig. 2(a) shows the waveforms of the applied voltage and total current for the discharge operating at a frequency of 50 kHz. The gas flow rate was kept constant at 1 L/min. For the applied voltage of amplitude 2.5 kV_{rms} (rms value), the peak total current was 0.26 A. The rms value of the discharge current was about 1 mA_{rms}. The voltage across the gas gap (V_g) is simply the difference between the applied voltage (V_a) and the voltage across the dielectric (V_d). Note that V_d follows temporally V_a with a time lag and the temporal profile of the total current resembles that of V_g, as shown in Fig. 2(a). The time lag is due to the charges from the plasma volume being collected on the surface of the dielectric [15]. To determine the actual discharge current [Fig. 2(b)], the displacement current (I_{no}) with plasma off was subtracted from the total current (I_{tot}).

Fig. 2(c) and (d) shows the temporal evolutions of the discharge current and the wavelength-integrated optical emission intensity for two types of outer tube nozzles mentioned above (a straight cylinder nozzle and a tapered nozzle, respectively). It was observed that the discharge produced at least two plasma bullets every cycle of the applied voltage, the main optical emission occurred at the rising edge of the positive half cycle of the voltage waveform, and the weak light emission signal occurred at the falling edge of the negative half cycle. The optical intensity measured at the electrode tip was found to be nearly in phase with the conduction current. However, the characteristics of light emission at the nozzle exit differ depending on the outer tube nozzle type. There is a difference in the phase of the optical intensity between the straight cylinder nozzle and the tapered nozzle jets, which may result from different drifting velocity of the charged species driven away from the electrode. The tapered nozzle jet has a larger optical intensity at the nozzle exit than the straight cylinder nozzle jet does.

The breakdown voltage was observed to be dependent on the diameter of the copper pin electrode (d_w) as: 1.13 kV_{rms} for 2 mm, 0.88 kV_{rms} for 1 mm, and 0.646 kV_{rms} for 0.5 mm. This can be attributed to the characteristics of corona discharges. In corona discharges, a charged conductor with a very small diameter of curvature, such as a sharp point or thin wire, can provide seed electrons to lower the gas breakdown voltage. Therefore, the discharge employing copper wire with a smaller diameter had a lower breakdown voltage, but at a fixed applied voltage above the breakdown voltage, the discharges mentioned above did not exhibit noticeable differences in the total current. Concerning the breakdown phenomena, the following were observed.

1) The breakdown voltage (and the plume-out voltage), the plume length, and the plume luminosity exhibited a quite strong dependence on the configurations of electrode and quartz tube for a fixed gas flow rate. The configurations of electrode and quartz tube include the distance between the copper pin and the exit of the outer quartz tube, the diameter of the copper pin, and the nozzle diameter.
2) The plasma jet with the bare copper pin electrode had a lower breakdown voltage.
3) In the case of the pin electrode inserted in the inner quartz tube, a thinner pin also resulted in a lower breakdown voltage.

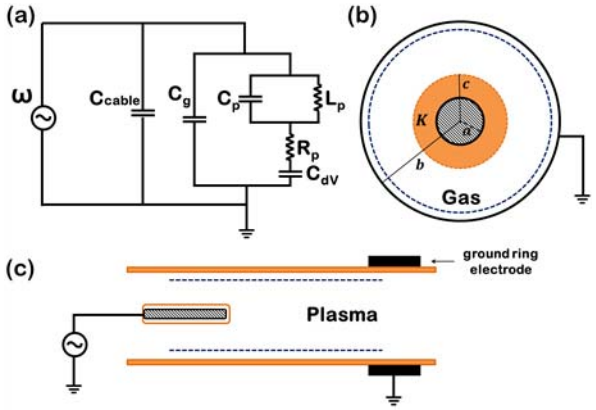

Fig. 3. (a) Equivalent circuit model of plasma jet. (b) Front view of the capacitance model for the pin electrode surrounded by the inner quartz tube (dielectric constant K) and the outer quartz tube. (c) Side view of the plasma jet. Dotted blue line represents a virtual electrode parallel to the grounded ring electrode over the inside surface of the outer tube.

The equivalent circuit model of the discharge used in our analysis is shown in Fig. 3(a). The capacitor C_{cable} represents the parasitic capacitance along with the cable capacitance of the power supply and additional electrical circuit components [16]. The impedance of plasma discharge is represented by a capacitor C_p, and an inductor L_p in parallel, and a resistor R_p, which is parallel to C_g (the equivalent capacitance of the gas gap and inner quartz tube surrounding the pin electrode). The R_p inversely depends on the conductivity of the gas in the current channel [15], C_p is related to the plasma sheath, and L_p is approximately R_p divided by the electron collision frequency. Based on the physics of the problem, we have imposed a virtual electrode [17], [18] parallel to the grounded electrode over the inside surface of the outer tube [blue dotted lines in Fig. 3(b) and (c)]. There is another capacitance C_{dv} between the virtual electrode and grounded electrode. The impedance of DBD plasma jet is essentially those of gas gap and of the plasma impedance with one capacitor C_{dv} in series. The total current is due to the combination of these circuit components.

Utilizing the capacitance of a coaxial cable shown in Fig. 3(b), the equivalent capacitance of the gas gap and inner quartz tube surrounding the pin electrode can be estimated as

$$C_g = \frac{2\pi\varepsilon_0 l}{\ln\left(\frac{b}{c}\right) + \frac{1}{K}\ln\left(\frac{c}{a}\right)} \tag{1}$$

where l is the length of the powered electrode; a, c, and b are radii of the pin electrode, inner quartz tube, and outer quartz tube, respectively; and K is the dielectric constant of the inner quartz tube. When the inner quartz tube is removed ($c \to a$ and $K \to 1$), the C_g is reduced to $C_{g0} = 2\pi\varepsilon_0 l/\ln(b/a)$. The equivalent resistance for the plasma part of the circuit driven by angular frequency (ω) is R_p, and the reactance is written

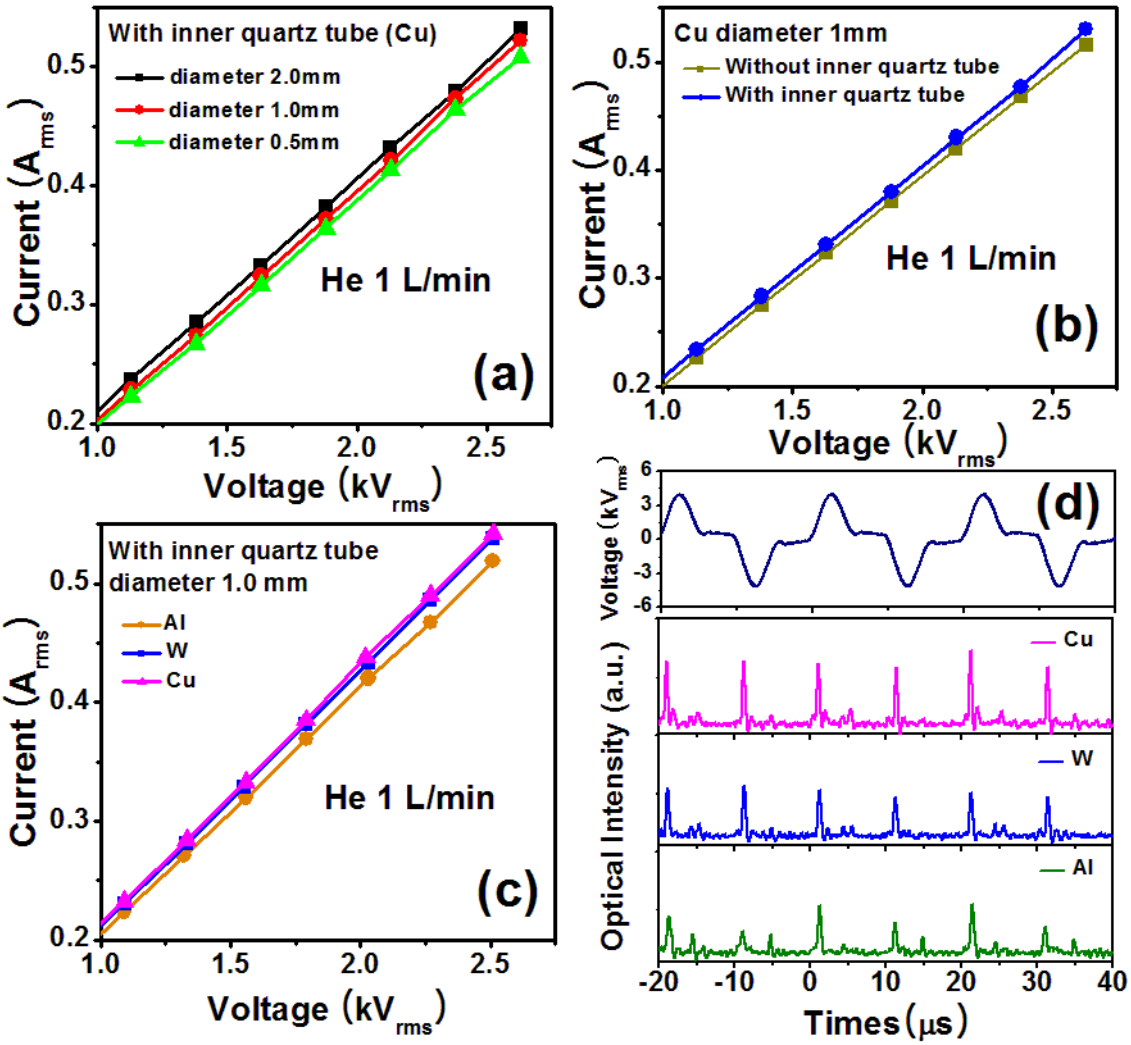

Fig. 4. (a) I–V curves of the plasma jets for different diameters of the copper pin. (b) I–V curves of the plasma jets with and without the inner quartz tube. (c) Comparison of I–V curves between the plasma jets with the Cu, W, and Al pin electrodes. (d) Comparison of wavelength-integrated optical intensity between the plasma jets with the Cu, W, and Al pin electrodes.

as [17]

$$X_1 = \frac{-L_p/C_p}{\omega L_p - 1/\omega C_p} - \frac{1}{\omega C_{dv}}. \tag{2}$$

The reactance associated with the capacitance between the powered electrode and grounded electrode C_g is given by $X_2 = -1/\omega C_g$. This is parallel to the impedance given by X_1. Based on the circuit, the equivalent resistance (R) and equivalent reactance (X) of the plasma jet are written as

$$R = \frac{X_2 R_p (X_1 + X_2) - X_1 X_2 R_p}{R_p^2 + (X_1 + X_2)^2}$$
$$X = \frac{X_2 R_p^2 + X_1 X_2 (X_1 + X_2)}{R_p^2 + (X_1 + X_2)^2} \tag{3}$$

where $R_p = \ln(b/c)/2\pi\sigma l$, and $\sigma = n_e e^2/m\nu_m$ is the plasma conductivity (n_e, e, and m are the number density, charge, and mass of electrons, respectively, and ν_m is the electron collision frequency. Because the attention in this paper is directed toward the electrical properties of the jet itself, the effect of the cable capacitance is not considered (in fact, the cable capacitance influences the current). In the low-frequency operation considered in this paper, the driving frequency is much lower than the electron collision frequency ($\omega \ll \nu_m$), and therefore, L_p is small and the first term X_1 in (2) is not significant. It is noted that if typical values of the circuit parameters are considered for the plasma jet in this paper (such as $\omega = 2\pi \times 10^5$, $C_p = 10$ pF, $L_p = 1$ pH, and $C_{\rm dv} = 1$ pF), $X_1 \backsim -1/\omega C_{\rm dv}$. If we even neglect the effective reactance of the plasma part ($X_1 = 0$) [14], the plasma impedance (Z_p) of the equivalent circuit can be simplified as

$$Z_p = \frac{R_p}{1 + \omega^2 R_p^2 C_g^2} + j\left(\frac{-\omega R_p^2 C_g}{1 + \omega^2 R_p^2 C_g^2}\right). \tag{4}$$

Fig. 4(a) shows the I–V curves for the plasma jets operated with three different diameters of the copper pin. The curves reveal that the plasma jet exhibits abnormal glow regions that are characteristic of weakly ionized plasmas. The applied voltage was in the range 0.6–2.6 $\rm kV_{rms}$, and the measured total current was 0.13–0.53 $\rm A_{rms}$. It was observed that the case of thicker copper pin had a larger total current, whereas it had

a longer plume. With an increase in the pin diameter, C_g is increased as easily seen in (1), resulting in a decrease of $|Z_p|$ according to (4) (an increase of the total current). This can also be explained by the decrease of plasma resistance due to the larger pin radius. The decrease in R_p implies an increase in the plasma density that leads to the increase in the plasma discharge current. As a result, the total plasma impedance $|Z_p|$ decreases (assuming that the reactance was little changed) and the total current increases. The results shown in Fig. 4(a) imply that the case of thicker copper pin has a slightly larger plasma density (lower plasma impedance). Although not shown in the figures, the length of the outer tube (L) did not make a significant difference in the I–V curve for the range 50–80 mm; however, the case of $L = 50$ mm had a slightly more intense plume. The internal diameter of the outer quartz tube (D) was influential in forming the plume and expelling it from the nozzle. The range of $D = 5$–6 mm was effective in the design and operation parameters of this paper (especially for the straight cylinder tube).

The total current versus the applied voltage for the different cases (with and without the inner quartz tube) is shown in Fig. 4(b). The presence of the inner quartz tube enhanced the total current. These can be explained in terms of (1) and (4). When there exists an inner quartz tube surrounding the pin electrode, C_g becomes larger than C_{g0} (the capacitance without the inner quartz tube). Then, $|X_2|$ is decreased, which results in the decreases of and R and $|X|$ in (3). The installment of the inner quartz tube affects R_p, C_p, and L_p (thus $|X_1|$) as well. Thus, the total impedance $|Z|$ changes in a complicated manner. The results indicate that with the inner quartz tube installed, $|Z|$ decreases slightly and the total current increases slightly. Because the external circuit remains the same, an increase in the observed total current leads to the increase in the discharge current. The reason for only small differences in the total current [Fig. 4(a) and (b)] is that the plasma jet in this paper has low discharge currents. This paper implies that when the discharge current becomes higher, noticeable differences are expected.

Because of the risk of arcing, the plasma plumes generated without the inner quartz tube are not the best for biomedical applications due to safety issues [12]. The inner quartz tube helps to reduce the danger of electric shock when one happens to touch the plume. Because the reactance of the inner quartz tube is much greater than that of humans, a considerable portion of the applied voltage is across the inner quartz tube, and thus, the voltage drop on the humans is small [14]. There are some concerns over the use of metallic electrodes in the plasma jet for material processing and biomedical applications, where copper atoms may prove to be detrimental [19]. To this end, encompassing the copper pin electrode by the inner quartz tube is desirable.

Fig. 4(c) and (d) shows the effect of the electrode material on the total current and optical intensity. Besides the copper electrode, tungsten and aluminum electrodes of the same dimension were considered. The copper electrode exhibited a slightly larger current and optical intensity than the other two electrodes. A larger optical intensity indicates a sufficient activation of neutral species by plasmas, which provides a well-suited environment for most of the relevant material processing and biomedical applications.

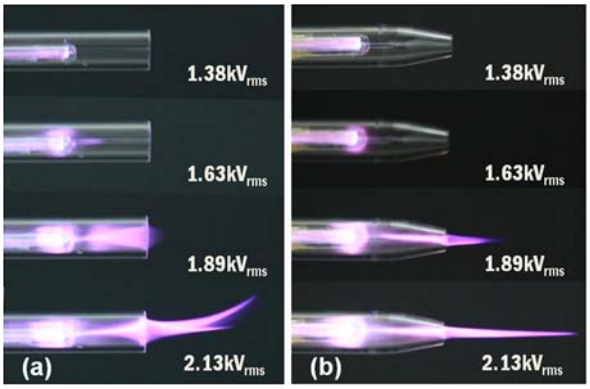

Fig. 5. Photographs of the plume and the plume length as a function of applied voltage in (a) straight cylinder type and (b) tapered type jets excited at 50 kHz (gas flow rate: 2 L/min).

The influence of the shape of outer quartz tube [a straight cylinder tube in Fig. 5(a) and a tapered tube in Fig. 5(b)] on the plume was also investigated. As shown in the figure, at a fixed gas flow rate, the gas speed becomes larger for the tapered-tube jet enabling the plume to be stable and well-focused and to reach further. Depending on the operating parameters, DBDs can generate either filamentary or diffuse plasmas. In the plasma jets of this paper, the application of higher voltages resulted in the filamentation of the plasmas in which many individual discharge channels were formed [see at 2.13 kV_{rms} in Fig. 5(a)]. This tendency was strong for thinner copper pin electrodes and bare copper pin electrodes.

The detailed studies have revealed that the cold plasma jet produced by nanosecond or microsecond pulsed discharges is typically composed of a series of rapidly propagating streamer discharges (plasma bullets). The length of the plasma plume (i.e., streamer propagation length) can be adjusted by the gas flow rate and the applied voltage. Fig. 6(a) and (b) shows the plume length of the straight cylinder jet as functions of applied voltage and gas flow rate for different diameters of the copper pin: 2 and 0.5 mm, respectively. The plume length, which is indicative of the distance plasma bullets can extend into the ambient atmosphere, is shown at the gas flow rates of 0.5–4 L/min. As expected, the plume length increased with the applied voltage. This trend was more dominant in the case of the thicker pin [Fig. 6(a)]. In particular, at applied voltages below 2.0 kV_{rms}, the jet with a 0.5-mm diameter copper pin had a longer plasma plume. In both cases, as the applied voltage increased, the jet front became unstable and filament like. As usual, the increase in the gas feeding resulted in jet elongation, while further increase (here, up to 5 L/min) in the flow rate caused jet shortening and appearance of a turbulent tail at the jet's end. Laminar mode is formed at low gas flow rates, while turbulent mode is produced at higher gas flow rates. The transition from laminar to turbulent mode is closely associated with a noticeable decrease of plasma jet length [20], [21]. The transition from laminar to turbulent mode can be detected by Reynolds number (R_e) defined as

$$R_e = \frac{V D}{v} \tag{5}$$

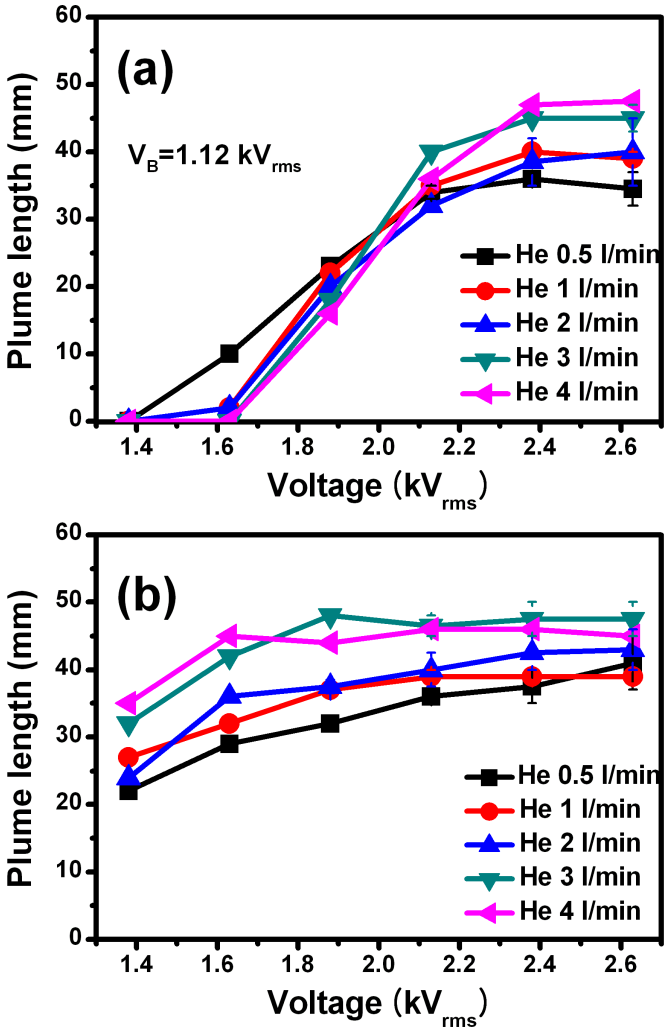

Fig. 6. Plume length of the straight cylinder type jet as a function of gas flow rate for different diameters of the copper pin (a) 2 and (b) 0.5 mm.

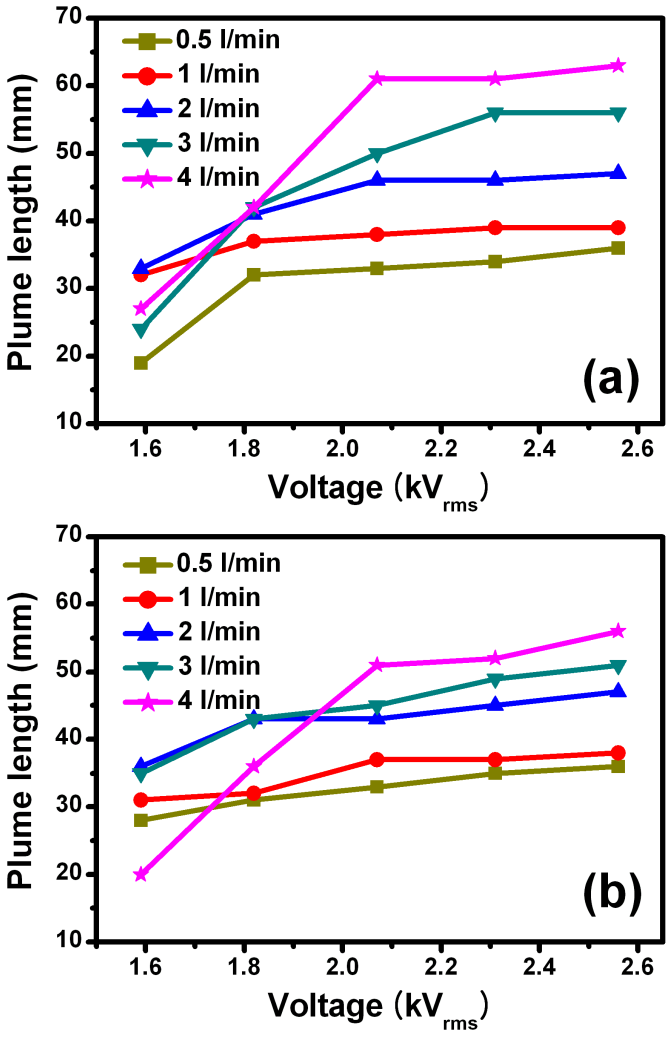

Fig. 7. Plume length as a function of applied voltage for different gas flow rates in tapered type jets: the tapering begins at (a) 5 and (b) 10 mm from the tube exit.

where ν is the kinematic viscosity, V is the gas flow velocity, and D is the nozzle diameter. For a typical operation condition (the gas flow rate of 2 L/min and nozzle diameter 5 mm), R_e is about 740. When R_e is above 2000, laminar mode progresses to turbulent mode. This transition point corresponds to the gas flow rate of 6 L/min, which is close to the experimental observation at the onset of turbulence.

Fig. 7 shows the plume length as functions of applied voltage and gas flow rates in tapered tube jets in which the tapering begins at (a) 5 and (b) 10 mm from the tube exit. In the jets with a tapered tube, a plasma plume extended up to more than 6 cm from the exit nozzle in the stable stage. A steeply tapered tube jet [Fig. 7(a)] was observed to have a longer plume than a smoothly tapered tube jet [Fig. 7(b)]. In the steeply tapered tube, the vortex structure of the helium flow became dominant and provided a longer gas residence time, enabling increased plasma activation. The plasma density was enhanced, and this led to the increase in the plasma plume length.

As can be observed in Fig. 7, the plasma plume length also increased with the gas flow rate for the range of the applied voltage above 2.0 kV_{rms}. In the laminar regime, an increase in the helium flow velocity resulted in a direct increase in the plasma plume length. The gas flow rate affected the variation of the plume length more significantly than the applied voltage did. This implies that in the tapered type jet, the plasma plume is largely governed by the gas flow [22]. As was seen in the straight cylinder jet, at higher gas flow rates, the plume from the tapered type jet also became unstable and the plume length began to decrease due to flow turbulence [23]. It can be concluded that the plume length is determined by several factors: applied voltage, outer quartz tube diameter, nozzle structure and diameter, and gas flow rate. In general, the plume length increases with: 1) an increase in the applied voltage; 2) a decrease in the outer quartz tube diameter; 3) an optimization of the nozzle size and tapering outer quartz tube; and 4) an increase in the gas flow rate.

B. Plume Temperature

Fig. 8 shows the measured plume temperature as functions of the operating parameters and the configuration variables. The plume temperature was measured using a fiber optic temperature sensor (Luxtron M601-DM&STF). A continuous increase in the plume temperature as the applied voltage increases was observed [Fig. 8(a)]. An increase in the applied

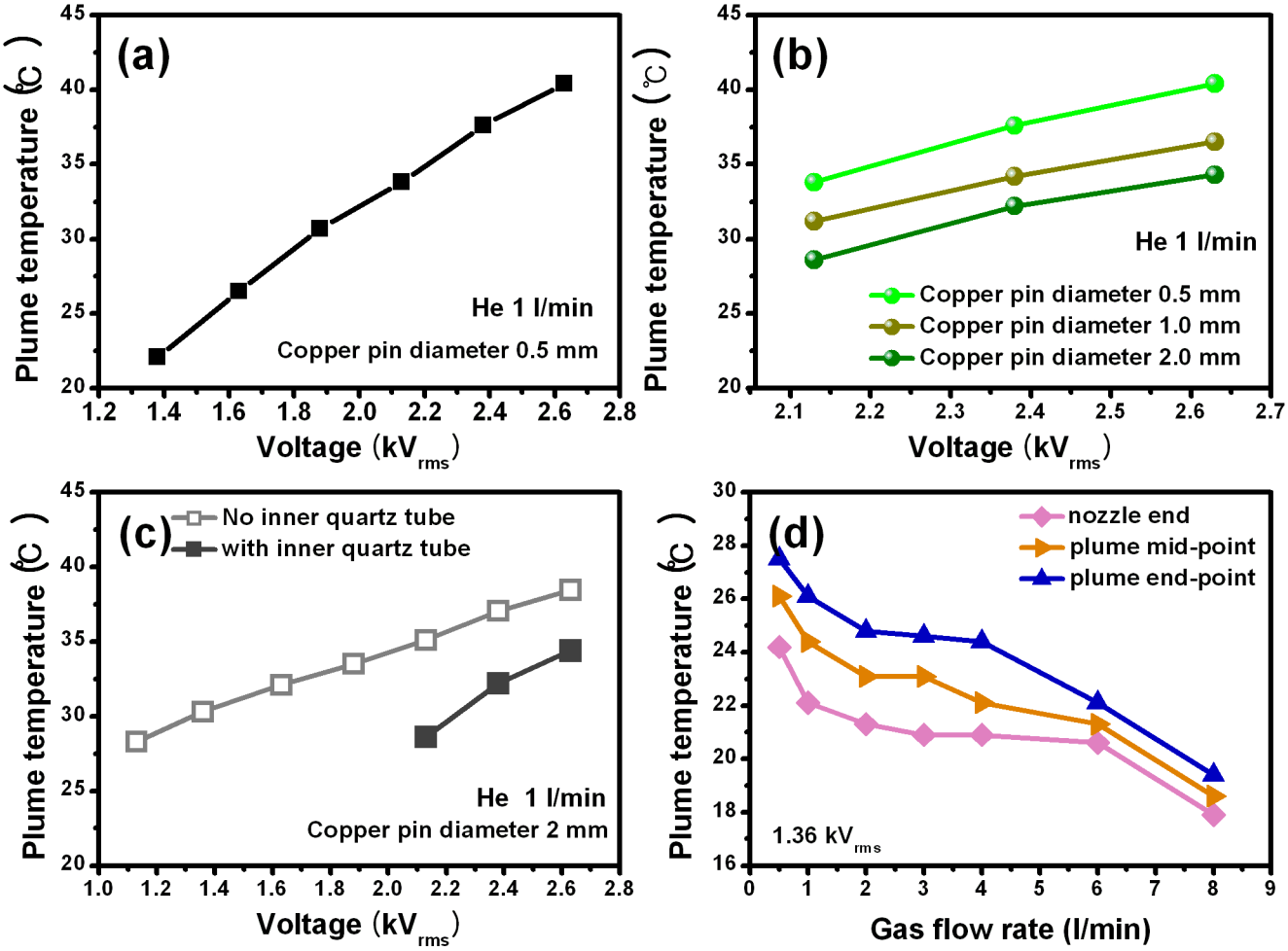

Fig. 8. Plume temperature as a function of (a) applied voltage, (b) applied voltage for different diameters of the copper pin, (c) applied voltage for the jets with and without the inner quartz tube, and (d) gas flow rate at different axial positions of the plume.

voltage leads to the increase of the plasma volume, which is immediately reflected by gas heating. When a thinner copper wire electrode was used, the plume temperature was found to increase because the effective electric field strength increased [Fig. 8(b)]. When the inner quartz tube encompassing the copper pin was employed, the plume temperature decreased [Fig. 8(c)]. This may be attributed to the fact that high-energy secondary electrons also contribute to gas heating in the case of bare copper pin electrodes.

The plume temperature depends on the plume current and the gas flow characteristics. The plume temperature was measured at various points—nozzle endpoint, plume midpoint, and plume end point—at different gas flow rates, as shown in Fig. 8(d). The plasma plume presented a low plume temperature near the nozzle in most discharge conditions, and the temperature rose slightly with the axial distance from the nozzle. The plume temperature was observed to decrease as the gas flow rate increased. These results indicate that the plume temperature can be effectively adjusted by controlling the gas flow rate [24].

C. Optical Characteristics

To identify reactive species that are generated in the discharge and subsequently expelled with the gas flow, spectra were recorded along the axis of the jet. The emission is collected perpendicular to the plume's propagating direction, and the distribution of emission intensities was obtained at different locations (see the points at the upright corner in Fig. 1) along the axial direction of the jets (for both the straight cylinder jet and the tapered jet). It should be noted that the emission intensity depends on the densities of the excited species and the surrounding electrons, the quenching rate, the emission characteristics (light frequency, spontaneous emission probability, and branching ratio), and the spectral response of the detection system. Therefore, it is difficult to infer the variation of species densities from the emission intensities. However, a given emission intensity from a species can be regarded as a measure of the concentration of the species for a qualitative analysis.

Fig. 9(a) and (b) shows the spatial distributions of selected emission intensities for the straight cylinder jet and the tapered jet (shown in the upright corner of Fig. 1), respectively. Although pure helium was injected in the tube as a working gas, nitrogen lines can be observed because the plasma is generated in ambient air, and therefore, nitrogen easily mixes at the nozzle exit. This shows that there are strong nitrogen molecular lines as well as a few helium and oxygen atomic lines. Oxygen and nitrogen species arise because the plasma

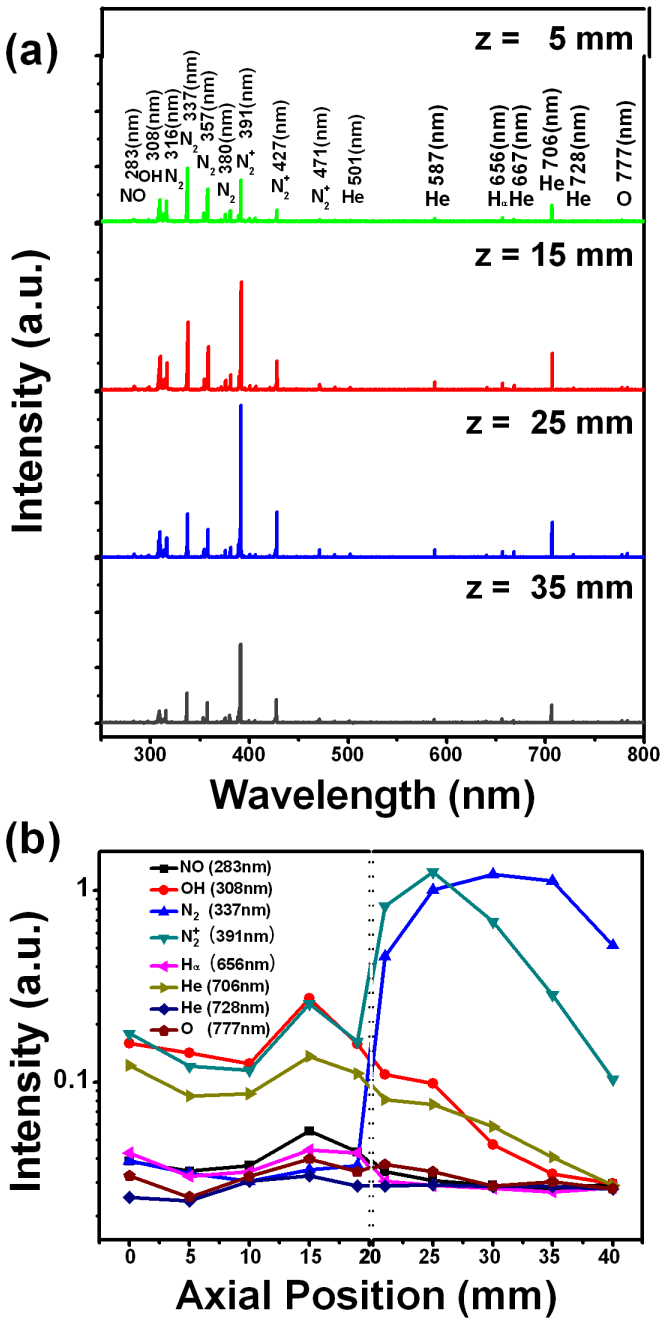

Fig. 9. Optical emission spectra at different positions along the axis for (a) straight cylinder type jet and (b) tapered type jet.

is ejected into the air where its energetic electrons and He metastables ionize and excite air molecules. The strongest emission was the N_2^* line at 337.1 nm ($C^3\Pi_u \rightarrow B^3\Pi_g$), and many nitrogen lines, excited He atom line at 706.5 nm, and excited oxygen line at 777.4 nm are shown. The N_2^+ line at 391 nm ($B^2\sum_u^+ \rightarrow X^2\sum_g^+$) is attributed to Penning ionization ($He^* + N_2 \rightarrow He + N_2^+ + e$) and charge transfer ($He^+ + N_2 \rightarrow He + N_2^+$) followed by direct electron-impact excitation ($e + N_2^+ \rightarrow N_2^{+*} + e$) [23]. Stronger excited N_2^+ emission was observed when a high voltage was applied (not shown in the figure). In the discharge area, the electron impact dissociation of N_2 and O_2 molecules leads to the formation of atomic oxygen and the breaking of the strong bond in the N_2 molecule by vibrational excitation and dissociation. Atomic oxygen may also be generated through Penning dissociation ($N_2^* + O_2 \rightarrow N_2 + O + O$). The emission line at 656 nm corresponds to the H_α line, which is generated by the collision between a water vapor molecule and electrons ($H_2O + e \rightarrow H + OH + e$). The emission spectrum clearly indicates that OH (309 nm) and NO (283 nm) exist in the plasma plume. The OH radicals are produced from water vapor in the helium flow, which is humidified by water adsorbed on the inner surface of the helium line and the quartz tube [25]. The presence of nitric oxide (NO) at 283 nm is due to the chemical conversion of N and O_2 (or N and O) [26]. The NO serves a multitude of essential biological functions, including the bactericidal effect and the induction of the phagocytosis of bacteria and necrotic detrite. These highly reactive species, such as O, OH, and NO are considered to be the most effective agents in attacking cells or organic material in general. The spectra obtained from inside the tube [Fig. 9(a)] reveal a predominance of excited He species with the He 706.5-nm line having the greatest intensity. The low intensity of the nitrogen second positive system with respect to the N_2^+ band is a feature of the He jets [13].

The spatial variation of the emission intensities from the excited species NO, O, OH, H_α, N_2, and N_2^+ along the axial direction can provide useful information on the properties of the plasma plume. As shown in Fig. 9(a), all the He lines that were studied (587.6, 667.8, 706.5, and 728 nm) had a similar pattern. Inside the outer quartz tube, emission from the nitrogen molecular ion (N_2^+) had a pattern similar to that of He lines [27], [28]. This can be explained by N_2^+ being formed in helium discharges through both Penning ionization and charge transfer, as mentioned above. Fig. 9(b) shows the axial variation of the line intensities from the tapered jet. In the figure, for convenient comparison between the intensity variations of various lines, the intensities of the two most intense lines (He 706.5 nm and O 777.4 nm) are displayed in arbitrary reduction, while that of OH (308 nm) line is a little magnified. The parallel double lines indicate the position of the nozzle exit. From the nozzle exit to ambient air, the lines of OH (309 nm) and He (706.5 nm) decrease. The lines of O (777.4 nm), H_α (656 nm), and NO (283 nm) also decrease slowly, while the lines of N_2 (337.1 nm) and N_2^+ (391 nm) exhibit an abrupt increase followed by a decrease. This phenomenon might be ascribed to the diffusion of the N_2 molecules into the He flow near the exit, enhancing the Penning ionization [9]. This feature is also in accord with [29]. Therefore, it is reasonable to conclude that the concentration of N_2^+ increases when the plasma exits the nozzle [30]. The spatial profiles of excited N_2 and N_2^+ show a good correlation with the axial gas temperature distribution [31]. The decrease in the concentrations of OH, NO, and H_α in the afterglow is mainly attributable to dilution of the feed gas in as much as these species are formed in the active zone of the discharge [26]. The OH emissions decayed immediately as soon as the plasma traveled out from the nozzle and decreases with distance from the nozzle [25]. The N_2 bands' emission volumes propagated to a far distance and formed the whole length of the helium plasma plume in the

surrounding air. The helium emissions decayed rapidly for the plasma inside and outside the nozzle due to the adverse effect of impurities, especially the large concentration of diffused air in the open space. These distinct types of dynamic behavior of the dispersed plasma emission volumes are attributable to the different generation and quenching mechanisms of their corresponding excited species [32]. This information allows determination of the optimum placement of the biological samples downstream of the plasma jet [29].

D. Effect of a Ground Ring Electrode

Finally, the effect of a ground ring electrode on the jet characteristics was explored. With this configuration, the electric field along the plasma plume is enhanced. Walsh and Kong's [3] studies show that a high electric field along the plasma plume is favorable for generating long plasma plumes and more active plasma chemistry. In addition, as observed from Fig. 10(a), the optical emission from the plasma between the two electrodes is much stronger than that of the plasma plume. Therefore, when touching the plume, the main part of the discharge current goes through the outer tube rather than the human. Therefore, the potential drop should be mainly between the electrodes and the potential drop on the human is further lowered [14].

The jet had a coaxial configuration with a central powered electrode and a grounded ring electrode with variable widths wrapped around the outer quartz tube. The distance between the ground ring electrode and the tip of the high voltage pin electrode was 40 mm, and the ground electrode was placed 20 mm away from the exit of the outer quartz tube. By wrapping a ground ring around the outer quartz tube, the equivalent interelectrode distance is decreased, thereby increasing the effective electric field. This enables an easy plasma ignition. For optimal operation of the jet, the optimal width and position of a ground ring around the quartz tube need to be determined. When the jet was operated with the applied voltages of 1.65 and 1.89 kV_{rms} and the gas flow rate of 2 L/min, the influence of the ring width was investigated and is clearly shown in Fig. 10. With the ground ring installed, the plume length, the total current, and the gas (plume) temperature exhibited increases compared with the case without the ring. As the ring width increased, the total current was observed to increase slightly (the plume length was not changed noticeably), and the gas temperature became higher due to increased Joule heating. With an increase in the ring width, C_{dv} is increased and $|X_1|$ is decreased in (2), which results in the decreases of R and $|X|$ in (3) (thus, an increase of the total current).

As shown in Fig. 11, the position of a ground ring influenced little on the total current, but influenced significantly on both the plume length and the plume temperature. Placing a ground ring near the tube exit made the effective electric field strength lower and resulted in a lower plume temperature. This result can be interpreted in terms of the reduced plasma density due to a reduced effective electric field strength, which leads to a consequent decrease of the plume temperature [33]. The capacitance due between the virtual electrode and grounded electrode (C_{dv}) is mainly influenced by the position of a ground ring. With an increase in the distance between the powered and grounded electrodes, C_{dv} is reduced and $|X_1|$ is increased in (2), which results in the increases of and R and $|X|$ in (3) (thus, a decrease of the total current). The gas

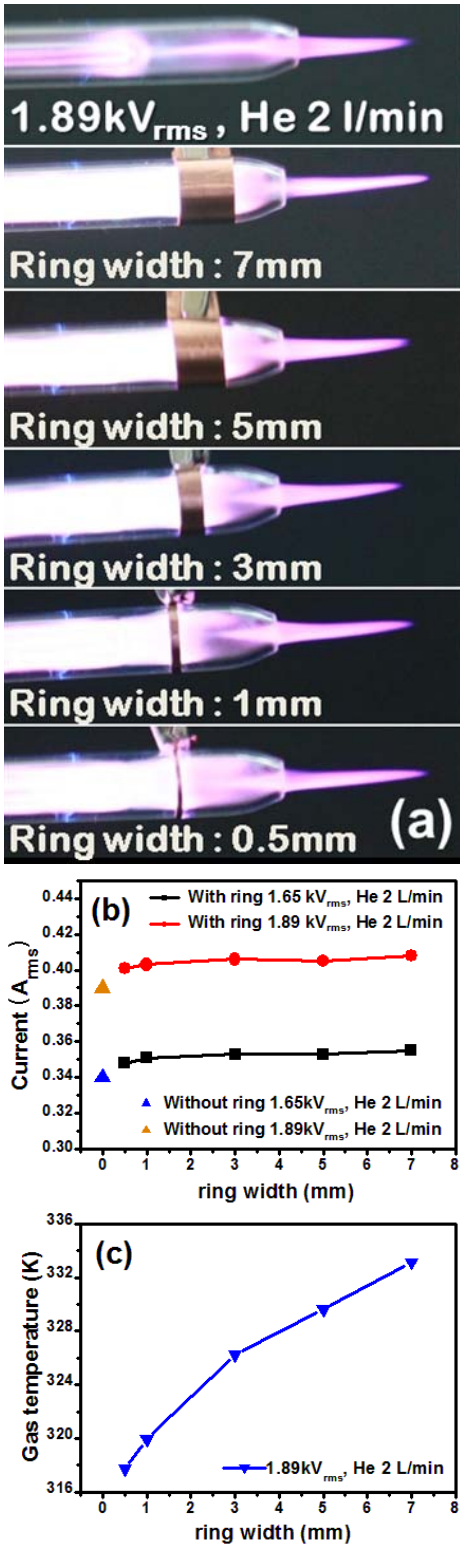

Fig. 10. Effects of the ground ring width. (a) Photographs of plume for different ring widths. (b) Total current. (c) Plume temperature as a function of the ring width.

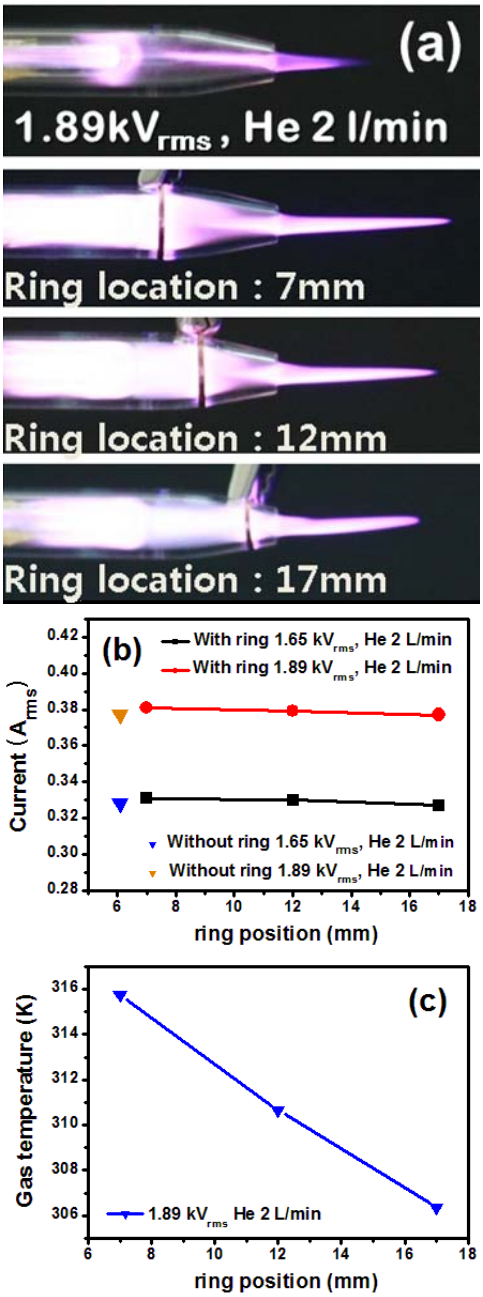

Fig. 11. Effects of the ground ring position. (a) Photographs of plume for different ring widths. (b) Total current. (c) Plume temperature as a function of the ring position.

gap capacitance (C_g) is also influenced by the position of a ground ring. With an increase in the distance between the electrodes (actually, this is equivalent to the increase of b), the C_g is decreased resulting in an increase of $|Z_p|$ (thus, in a decrease of the total current) according to (4) (in the region of $R_p \ll 1/(\omega C_g)$). Therefore, to achieve a low plume temperature, a narrower ground ring should be located near the tube exit.

IV. Conclusion

Atmospheric-pressure helium plasma jets excited by a low-frequency pulsed bipolar source were fabricated and characterized. The plasma plumes were generated reaching several centimeters near room temperature without any electrical shock. A variety of choices in the design configuration, including the electrode material and operation parameters, were undertaken to determine optimal conditions well suited for material processing or biomedical applications and to elucidate the properties of the plasma jets. The inner quartz tube surrounding the pin electrode and two kinds of outer quartz tubes (straight cylinder or tapered ends) were employed and tested. The breakdown voltage, the plume length, and the plume luminosity exhibited quite a strong dependence on the configurations of electrode (and tube) and gas flow rate. As for the breakdown voltage and the plume length, it was observed that: 1) the plasma jets with thinner diameter pin electrode had a lower breakdown voltage; 2) the plasma jet with the bare copper pin electrode had a lower breakdown voltage; and 3) the plume length increased with: a) an increase in the applied voltage; b) a decrease in the outer quartz tube diameter; c) an optimization of the nozzle size and tapering outer quartz tube; and d) with an increase in the gas flow rate. The variation of the emission intensities from the excited species NO, O, OH, N_2, and N_2^+ along the axial direction of the jet can provide useful information on the properties of the plasma plume. In addition, the influences of the position and width of a ground ring on the plume properties (length and temperature) and on the total current were explored to determine optimal operation of the jet. The electrical characteristics of the jet were found to be well explained by the equivalent circuit model of the discharge.

References

[1] M. Laroussi and T. Akan, "Arc-free atmospheric pressure plasma jets: A review," *Plasma Process. Polym.*, vol. 4, no. 9, pp. 777–788, Nov. 2007.
[2] J. L. Walsh, F. Iza, N. B. Janson, V. J. Law, and M. G. Kong, "Three distinct modes in a cold atmospheric pressure plasma jet," *J. Phys. D, Appl. Phys.*, vol. 43, no. 7, p. 075201, Feb. 2010.
[3] J. L. Walsh and M. G. Kong, "Contrasting characteristics of linear-field and cross-field atmospheric plasma jets," *Appl. Phys. Lett.*, vol. 93, no. 11, p. 111501, Sep. 2008.
[4] M. Teschke, J. Kedzierski, E. G. Finantu-Dinu, D. Korzec, and J. Engemann, "High-speed photographs of a dielectric barrier atmospheric pressure plasma jet," *IEEE Trans. Plasma Sci.*, vol. 33, no. 2, pp. 310–311, Apr. 2005.
[5] A. Fridman, A. Chirokov, and A. Gutsol, "Non-thermal atmospheric pressure discharges," *J. Phys. D, Appl. Phys.*, vol. 38, no. 2, pp. R1–R24, Jan. 2005.
[6] X. T. Deng and M. G. Kong, "Frequency range of stable dielectric-barrier discharges in atmospheric He and N_2," *IEEE Trans. Plasma Sci.*, vol. 32, no. 4, pp. 1709–1715, Aug. 2004.
[7] G. A. Dawson and W. P. Winn, "A model for streamer propagation," *Zeitschrift Phys.*, vol. 183, no. 2, pp. 159–171, 1965.
[8] X. Duan, F. He, and J. Ouyang, "Prediction of atmospheric pressure glow discharge in dielectric-barrier system," *Appl. Phys. Lett* , vol. 96, no. 23, p. 231502, Jun. 2010.
[9] R. Ye and W. Zheng, "Temporal-spatial-resolved spectroscopic study on the formation of an atmospheric pressure microplasma jet," *Appl. Phys. Lett.*, vol. 93, no. 7, p. 071502, Jul. 2008.
[10] E. Karakas, M. A. Akman, and M. Laroussi, "The evolution of atmospheric-pressure low-temperature plasma jets: Jet current measurements," *Plasma Sour. Sci. Technol.*, vol. 21, no. 3, p. 034016, May 2012.
[11] J. Jarrige, M. Laroussi, and E. Karakas, "Formation and dynamics of plasma bullets in a non-thermal plasma jet: Influence of the high-voltage parameters on the plume characteristics," *Plasma Sour. Sci. Technol.*, vol. 19, no. 6, p. 065005, Oct. 2010.
[12] X. Lu, M. Laroussi, and V. Puech, "On atmospheric-pressure non-equilibrium plasma jets and plasma bullets," *Plasma Sour. Sci. Technol.*, vol. 21, no. 3, p. 034005, May 2012.

[13] H. S. Park, S. J. Kim, H. M. Joh, T. H. Chung, S. H. Bae, and S. H. Leem, "Optical and electrical characterization of an atmospheric pressure microplasma jet with a capillary electrode," *Phys. Plasmas*, vol. 17, no. 3, p. 033502, Mar. 2010.

[14] X. Lu, Z. Jiang, Q. Xiong, Z. Tang, X. Hu, and Y. Pan, "An 11 cm long atmospheric pressure cold plasma plume for applications of plasma medicine," *Appl. Phys. Lett.*, vol. 92, no. 8, p. 081502, Feb. 2008.

[15] M. Laroussi, X. Lu, V. Kolobov, and R. Arslanbekov, "Power consideration in the pulsed dielectric barrier discharge at atmospheric pressure," *J. Appl. Phys.*, vol. 96, no. 5, pp. 3028–3030, Sep. 2004.

[16] U. N. Pal *et al.*, "Electrical modelling approach for discharge analysis of a coaxial DBD tube filled with argon," *J. Phys. D, Appl. Phys.*, vol. 42, no. 9, p. 045213, Jan. 2009.

[17] K. P. Singh and S. Roy, "Impedance matching for an asymmetric dielectric barrier discharge plasma actuator," *Appl. Phys. Lett.*, vol. 91, no. 8, p. 081504, Aug. 2007.

[18] Y. Hong, N. Lu, J. Pan, J. Li, Y. Wu, and K. F. Shang, "Characteristic study of cold atmospheric argon plasma jets with rod-tube/tube high voltage electrode," *J. Electrostatics*, vol. 71, no. 2, pp. 93–101, Apr. 2013.

[19] J. L. Walsh and M. G. Kong, "Portable nanosecond pulsed air plasma jet," *Appl. Phys. Lett.*, vol. 99, no. 8, p. 081501, Aug. 2011.

[20] Y. S. Seo, A.-A. H. Mohamed, K. C. Woo, H. W. Lee, J. K. Lee, and K. T. Kim, "Comparative studies of atmospheric pressure plasma characteristics between He and Ar working gases for sterilization," *IEEE Trans. Plasma Sci.*, vol. 38, no. 10, pp. 2954–2962, Oct. 2010.

[21] D. J. Jin, H. S. Uhm, and G. Cho, "Influence of the gas-flow Reynolds number on a plasma column in a glass tube," *Phys. Plasmas*, vol. 20, no. 8, p. 083513, Aug. 2013.

[22] Y. B. Xian, X. Lu, S. Wu, P. K. Chu, and Y. Pan, "Are all atmospheric pressure cold plasma jets electrically driven?" *Appl. Phys. Lett.*, vol. 100, no. 12, p. 123702, Mar. 2012.

[23] W.-C. Zhu, Q. Li, X.-M. Zhu, and Y.-K. Pu, "Characteristics of atmospheric pressure plasma jets emerging into ambient air and helium," *J. Phys. D, Appl. Phys.*, vol. 42, no. 20, p. 202002, Sep. 2009.

[24] T. L. Ni, F. Ding, X. D. Zhu, X. H. Wen, and H. Y. Zhou, "Cold microplasma plume produced by a compact and flexible generator at atmospheric pressure," *Appl. Phys. Lett.*, vol. 92, no. 24, p. 241503, Jun. 2008.

[25] S. Yonemori, Y. Nakagawa, R. Ono, and T. Oda, "Measurement of OH density and air-helium mixture ratio in an atmospheric-pressure helium plasma jet," *J. Phys. D, Appl. Phys.*, vol. 45, no. 22, p. 225202, May 2012.

[26] X. L. Deng, A. Yu, A. Y. Nikiforov, P. Vanraes, and C. Leys, "Direct current plasma jet at atmospheric pressure operating in nitrogen and air," *J. Appl. Phys.*, vol. 113, no. 2, p. 023305, Jan. 2013.

[27] Q. Xiong *et al.*, "Temporal and spatial resolved optical emission behaviors of a cold atmospheric pressure plasma jet," *J. Appl. Phys.*, vol. 106, no. 8, p. 083302, Oct. 2009.

[28] F. J. Andrade *et al.*, "A new, versatile, direct-current helium atmospheric-pressure glow discharge," *J. Anal. Atomic Spectrom.*, vol. 21, no. 11, pp. 1175–1184, Oct. 2006.

[29] E. Karakas, A. Munyanyi, L. Greene, and M. Laroussi, "Destruction of α-synuclein based amyloid fibrils by a low temperature plasma jet," *Appl. Phys. Lett.*, vol. 97, no. 14, p. 143702, Oct. 2010.

[30] Z. Xiong, X. Lu, Y. Xian, Z. Jiang, and Y. Pan, "On the velocity variation in atmospheric pressure plasma plumes driven by positive and negative pulses," *J. Appl. Phys.*, vol. 108, no. 10, p. 103303, Nov. 2010.

[31] S. Wang, V. Schulz-von der Gathen, and H. F. Dobele, "Discharge comparison of nonequilibrium atmospheric pressure Ar/O_2 and He/O_2 plasma jets," *Appl. Phys. Lett.*, vol. 83, no. 16, pp. 3272–3274, Oct. 2003.

[32] Q. Xiong, A.Y. Nikiforov, X. P. Lu, and C. Leys, "High-speed dispersed photographing of an open-air argon plasma plume by a grating-ICCD camera system," *J. Phys. D, Appl. Phys.*, vol. 43, no. 41, p. 415201, Aug. 2010.

[33] D. Mariotti, "Nonequilibrium and effect of gas mixtures in an atmospheric microplasma," *Appl. Phys. Lett.*, vol. 92, no. 15, p. 151505, Apr. 2008.

Authors' photographs and biographies not available at the time of publication.